Nano Research
2021, 14(7): 2231–2240
ISSN 1998-0124 CN 11-5974/O4
https://doi.org/10.1007/s12274-020-3204-z

Research Article

Self-exothermic reaction driven large-scale synthesis of phosphorescent carbon nanodots

Shi-Yu Song[1,§], Lai-Zhi Sui[2,§], Kai-Kai Liu[1] (✉), Qing Cao[1], Wen-Bo Zhao[1], Ya-Chuan Liang[1], Chao-Fan Lv[1], Jin-Hao Zang[1], Yuan Shang[1,3] (✉), Qing Lou[1], Xi-Gui Yang[1], Lin Dong[1], Kai-Jun Yuan[2], and Chong-Xin Shan[1] (✉)

[1] *Henan Key Laboratory of Diamond Optoelectronic Materials and Devices, School of Physics and Microelectronics, Zhengzhou University, Zhengzhou 450052, China*
[2] *State Key Laboratory of Molecular Reaction Dynamics, Dalian Institute of Chemical Physics, Chinese Academy of Sciences, 457 Zhongshan Road, Dalian 116023, China*
[3] *Super Computer Center, Smart City Institute, Zhengzhou University, Zhengzhou 450001, China*
[§] *Shi-Yu Song and Lai-Zhi Sui contributed equally to this work.*

Received: 26 August 2020 / **Revised:** 14 October 2020 / **Accepted:** 16 October 2020

ABSTRACT

Phosphorescent carbon nanodots (CNDs) have various attractive properties and potential applications, but it remains a formidable challenge to achieve large-scale phosphorescent CNDs limited by current methods. Herein, a large-scale synthesis method for phosphorescent CNDs has been demonstrated via precursors' self-exothermic reaction at room temperature. The as-prepared CNDs show fluorescence and phosphorescence property, which are comparable with that synthesized by solvothermal and microwave method. Experimental and computational studies indicate that exotic atom doped sp^2 hybridized carbon core works as an emissive center, which facilities the intersystem crossing from singlet state to triplet state. The CNDs show phosphorescence with tunable lifetimes from 193 ms to 1.13 s at different temperatures. The demonstration of large-scale synthesis of phosphorescent CNDs at room temperature opens up a new window for room temperature fabrication phosphorescent CNDs.

KEYWORDS

carbon nanodots, phosphorescence, large scale, self-exothermic reaction

Introduction

Room temperature phosphorescent (RTP) materials including heavy metal-based inorganics, organometallic complexes, or metal-free pure organic RTP molecules etc. [1, 2] have been developed because of their long-lived excited state electrons, which have great scientific significance and application perspective in many fields, including bioimaging, optoelectronic devices, information security, and so on [3–7]. RTP materials containing heavy atoms are faced with high-cost, toxicity, and complicated synthesis process. In addition, most of RTP materials are synthesized in elevated temperature, and this will hinder the mass production in view of practical applications. In recent years, developing emissive nanomaterials especially at room temperature condition is fascinating [8, 9], which provides a good reference for development large-scale synthesis of eco-friendly phosphorescent nanomaterials at room temperature.

As a new type of luminescent material, functional carbon nanodots (CNDs) have aroused increasing attention due to their high photoluminescence yields [10], good biocompatibility [11–13], and low toxicity [14–16], which are favorable for applications in the field of bioimaging [17–20], photodynamic therapy [21], photoelectric devices [22–25], information security encryption [26–28] and so on. A series of methods including hydrothermal and microwave-assisted synthesis have been developed to synthesize RTP CNDs [27, 29, 30]. Typically, in the reaction process, the synthesis temperature is around or over 180 °C and the reaction time of two or more hours is needed for the formation of RTP CNDs [31–36]. This method has advantage of easy accessibility, but the negative aspects are equally notable. Firstly, high temperature is inevitable in the process, this will increase energy cost. Secondly, solvent used in these processes will inevitably participate in the formation of RTP CNDs, increasing the difficulty of separation and purification and will limit production scale. Therefore, developing a facile, rapid, and large-scale synthesis route for RTP CNDs at room temperature condition is needed. But, there still have a great challenge because the carbonization process in the formation of CNDs must be proceeded at high temperature.

In this work, we report a facile and large-scale synthesis strategy to prepare phosphorescent RTP CNDs at room temperature for the first time, giving a production of 45 g within 5 min and a comparably high yield of 90%. The precursors phthalic anhydride and ethylene diamine spontaneous give off a lot of heat when they meet, and they will further undergo the process of self-crosslink and carbonization to form the phosphorescent CNDs. Interestingly, the CNDs show tunable phosphorescent lifetimes from 193 ms to 1.13 s (273–77 K) at

Address correspondence to Kai-Kai Liu, liukaikai@zzu.edu.cn; Yuan Shang, doctorshangyuan@gmail.com; Chong-Xin Shan, cxshan@zzu.edu.cn

different temperatures, and information encryption based on the CNDs has been demonstrated.

Results and discussion

The formation of CNDs must involve carbonization process, thus to achieve phosphorescent CNDs at room temperature, precursors used for CNDs must give off a lot heat to complete carbonization process [37, 38]. Phthalic anhydride and ethylene diamine were selected as carbon source to produce CNDs in view of the exothermic reaction between them. As shown in Fig. 1(a), by adding ethylene diamine in the phthalic anhydride dropwise under stirring, the temperature of the mixture increases rapidly and obviously because of the heat given off during the reaction process. Especially, the temperature increases from 26 to about 106 °C quickly within 60 s and the temperature decreases gradually in the next 600 s, the detailed change of temperature versus time was recorded in Fig. S1 in the Electronic Supplementary Material (ESM) . In this process, an intermediate (2-(2-aminoethyl) isoindoline-1,3-dione) formed due to the dehydration condensation between two precursors during the spontaneous exothermic reaction process, then the intermediate further underwent self-crosslink and carbonization process to form the phosphorescent CNDs with sp^2 @ sp^3 structure as illustrated in Fig. 1(b). The structure and orbitals of the CNDs are shown in Fig. 1(c). The sp^2 hybridized carbon core domain of the CNDs is constituted of phthalic anhydride; the sp^3 hybridized chains are constituted of ethylene diamine that containing sp^3 hybridized carbon and nitrogen atoms. The orbitals of the CNDs contain p-conjugated orbitals provided by sp^2 carbon atoms and non-bonding (n) orbitals provided by oxygen and nitrogen atoms. The (n, π*) states make the CNDs effective non-radiative recombination between the singlet and triplet excited state, thus phosphorescence can be observed at room temperature. The electrons transitions of the CNDs involved process of phosphorescence are shown in Fig. 1(d), and the molecular formulas of the precursor and intermediate are shown in Fig. 1(e). For the phosphorescence process, the intersystem crossing (ISC) between singlet and triplet states are promoted by spin-orbit coupling (SOC). According to the El-Sayed rule, effective SOC occurs in the transition from excited state configuration ^{1}(n, π*) to ^{3}(π, π*) or (π, π*) or ^{3}(n, π*) due to the effectively overlap [39, 40]. For the CNDs, the presence of n orbitals provided by oxygen and nitrogen atoms perpendicular to orbitals of the CNDs are favor of ISC from singlet to triplet states [36, 41, 42]. After cessation of excitation light, non-radiative recombination ISC occurs between S_1 state and T_1 state and photons are emitted by radiative recombination between T_1 and S_0 state.

The self-exothermic reaction driven synthesis strategy can large-scale prepare phosphorescent RTP CNDs with a production of 45.8 g at room temperature, as shown in Fig. 2(a). The morphological and structural properties of the CNDs were characterized in order to investigate their structure-function relationship. Transmission electron microscopy (TEM) and atomic force microscopy (AFM) were used to characterize the morphology and height of the CNDs. Figures 2(b) and 2(c) show TEM and AFM images of the CNDs, respectively. The

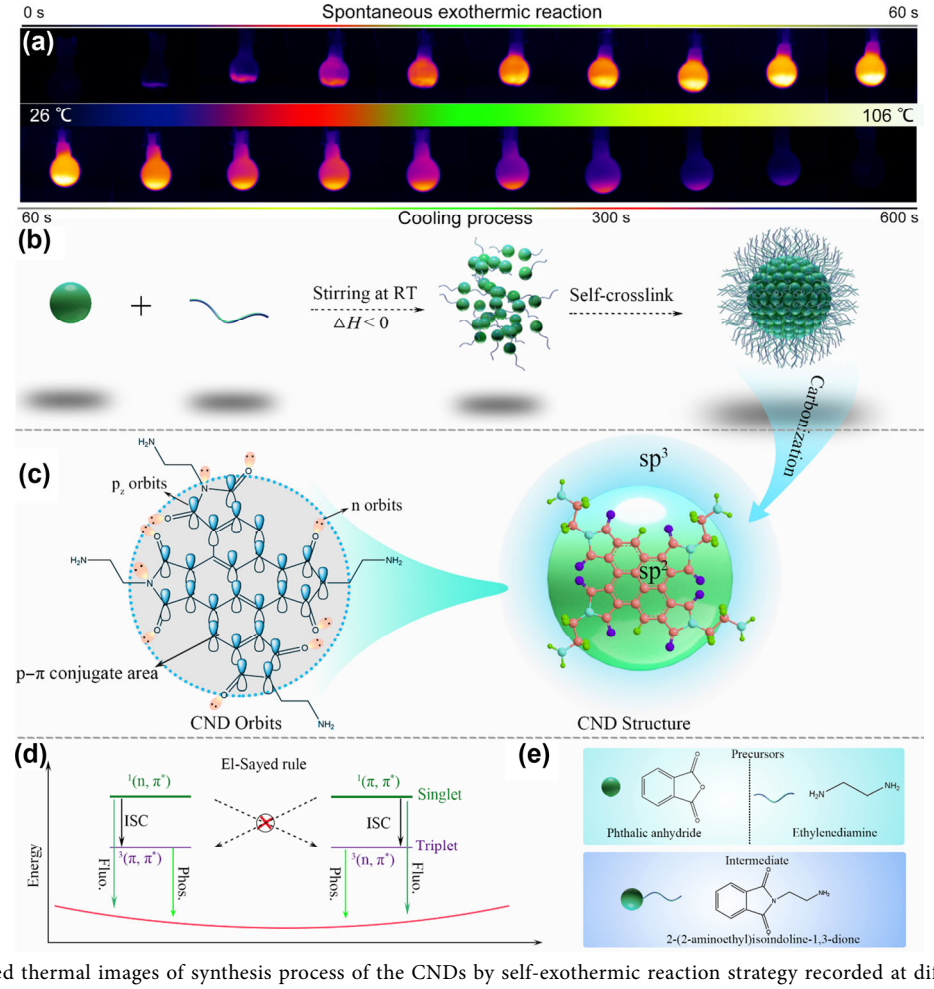

Figure 1 (a) Infrared thermal images of synthesis process of the CNDs by self-exothermic reaction strategy recorded at different time intervals, respectively. (b) Schematic diagram of the formation of the CNDs at room temperature. (c) The structure and electron orbitals of the CNDs. (d) Schematic illustration of EI-Sayed rule. (e) Precursors' structure and name.

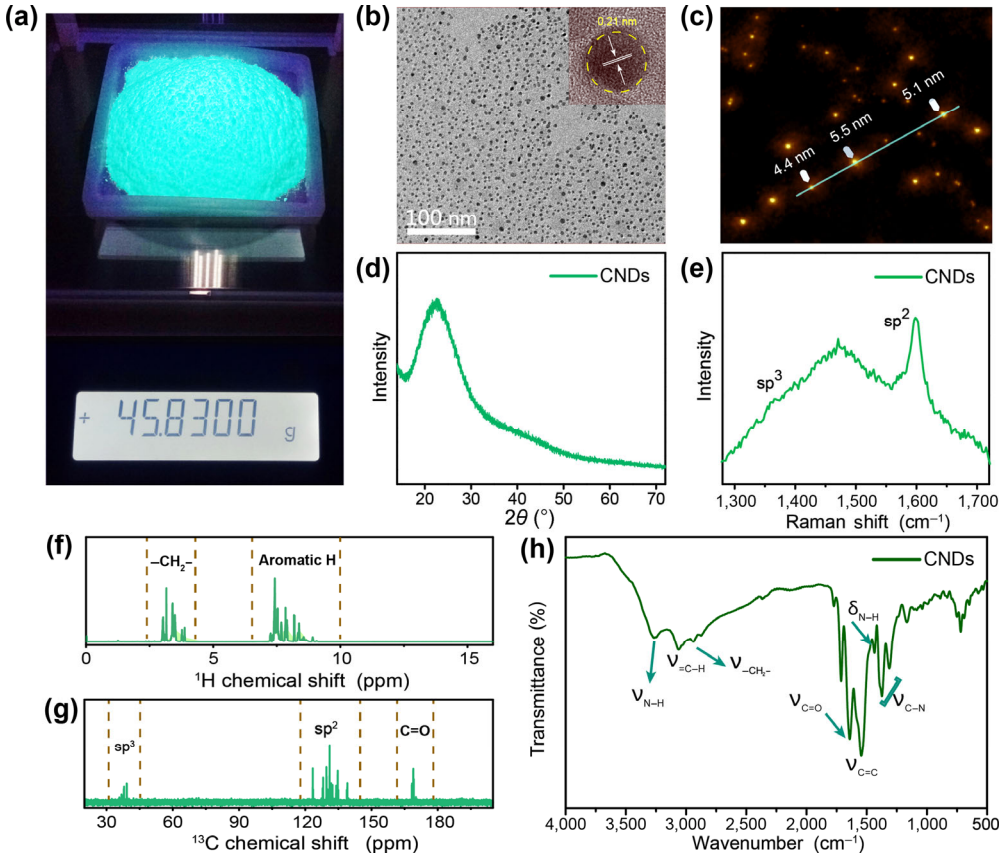

Figure 2 (a) The image of the as-prepared CNDs powders. (b) TEM image of the CNDs, the insert image is HRTEM image. (c) AFM image of the CNDs. (d) XRD pattern and (e) Roman spectrum of the CNDs. (f) ^{13}C NMR spectrum of the CNDs. (g) ^{1}H spectrum of the CNDs. (h) The FTIR spectrum of the CNDs.

as-prepared CNDs show uniform dispersion without aggregation. The insert image in Fig. 2(b) discloses the crystalline nature with a lattice space of 0.21 nm. The particle size distribution of the CNDs obeys a Gaussian distribution with a mean size of 4 nm (Fig. S2 in the ESM). AFM image (Fig. 2(c)) of the CNDs reveals that their height is in range of 4.4–5.5 nm, which indicates the CNDs have a sphere-like morphology. The X–ray diffraction (XRD) pattern in Fig. 2(d) shows two peaks at 25° and a weak signal at 43°, which are the typical peaks of graphite structure [43]. Figure 2(e) shows the Raman spectrum of the CNDs, it exhibits two peaks at 1,354 and 1,598 cm^{-1}, corresponding to the disordered (D band) and graphite (G band) of carbon materials [44]. It is known that the ratio of I_G/I_D is characteristic of the extent of graphite and the ratio of sp^2/sp^3 carbon. The ratio of I_G/I_D is 1.2, which is higher than the most CNDs, confirming the high degree of crystallinity of the CNDs. Moreover, ^{1}H nuclear magnetic resonance (^{1}H NMR) and ^{13}C NMR spectra were recorded, as shown in Figs. 2(f) and 2(g). ^{1}H NMR gave a set of peaks in the aliphatic region (δ = 2.92–3.96 ppm) and the alkene region (δ = 7.14–8.82 ppm). In the ^{1}H NMR spectrum, the high density of sharp signals in the range of 2–5 ppm is related to the presence of saturated aliphatic hydrocarbon, while the signals in the range of 7–9 ppm correspond to hydrogen atoms of benzene ring [45]. In the ^{13}C NMR spectrum (Fig. 2(g)), signals in the range of 30–40 ppm correspond to aliphatic (sp^3) carbon atoms. The signals in the range of 170–180 ppm correspond to carbonyl groups. In addition, the resonance signals in the range of 120 to 145 ppm are indicative of the sp^2 carbon atoms, indicating the formation of sp^2 domains during the synthesis of the CNDs. Fourier-transform infrared (FTIR) spectrum also recorded, as shown in Fig. 2(h). By comparing the FTIR spectra of the CNDs, one can see that the spectrum of the CNDs has characteristic absorption peak at around 3,450 cm^{-1}, which can be assigned to the stretching vibration of –NH. The peak at 3,065 cm^{-1} can be assigned to C–H vibration of aromatic ring (sp^2 carbon atom), while the peak at 2,936 cm^{-1} is C–H vibration of sp^3 carbon atom [46, 47]. The peak at 1,529 cm^{-1} can be ascribed to aromatic stretching vibration of graphite domains. The typical peak at 1,650 cm^{-1} is associated with the bending vibrations of –C=O. The peak at 1,479 cm^{-1} is related to the stretching of C–N. The above results indicate that the inside structure of the CNDs is made up of sp^2-hybrided carbon atoms, and surface structure mainly contained sp^3-hybrided carbon atoms. The calculated FTIR spectra of the configurations and the FTIR spectra of the CNDs experimentally measured are shown in Fig. S3 in the ESM. The peaks of the functional groups (–NH$_2$, –C=O, and C–N) can be observed from the calculated spectra of configurations, which agree with the measured FTIR spectrum of the CNDs. These observations also indicate the formation of polyaromatic structures in the CNDs during the reaction process. In order to explore the exact structure of the CNDs further, the samples were etched by argon plasma for 10, 20, and 40 s to remove any possible surface contamination before the XPS measurement, as presented in Fig. S4 in the ESM. The full XPS spectra include three typical peaks: C 1s (284.6 eV), N 1s (398.4 eV), and O 1s (531.8 eV), revealing the CNDs mainly contain the mentioned elements [48, 49]. The XPS spectra without etching show that the surface layer of the CNDs is mainly composed of carbon (67.59%), nitrogen (10.74%), and oxygen (21.67%), as shown in Fig. S5 in the ESM. While after etching for 10, 20, and 40 s, sp^2/sp^3 carbons (C=C/C–C, 284.3 eV), nitrous carbons (C–N, 285.4 eV), amide carbons (C=O, 287.8 eV) are observed

from C 1s spectrum, as indicated in Figs. S4(a) and S4(c) in the ESM. The high-resolution spectrum of N 1s displays two peaks at 398.4 and 400.3 eV, which can be attributed to pyrrolic N and, amino N, respectively. The C=O peak at 531.1 eV can be observed in O 1s spectrum. The inner structure of the CNDs is mainly composed of carbon, nitrogen and oxygen, as shown in Fig. S4(f) in the ESM. The C–N in the inner part of the CNDs increase significantly as the etching time increases, indicating that the C–N together with the sp^2-bonded carbon constitute the stable internal carbon core of the CNDs. The functional groups passivate the carbon core of the CNDs, making them have excellent fluorescence emission behavior. This behavior can be explained by the defects in the CNDs due to the incorporation of nitrogen atoms or oxygen atoms to the sp^2 scaffold. Based on all the above results, we proposed a possible mechanism for the formation of the CNDs: precursor anhydride undergoes polymerization and dehydration reaction with ethylene diamine, the reaction releases a large amount of heat rapidly to further carbonize the CNDs and then a carbonization core consisting of the nitrogen atoms together with a large sp^2 domain was formed, and many functional group (C=O, $-NH_2$) chains remained linked to the carbon cores.

In order to get a deeper understanding of the relationship between the carbon structure and the optical properties, the electronic and optical properties of computationally tractable models of CNDs configurations were evaluated using the first-principles density functional theory (DFT). Band gap energy (The lowest unoccupied molecular orbital (LUMO) and the highest occupied molecular orbital (HOMO) energy gap derived from first-principles calculations using DFT based methods) is consistent with the energy relative to the peak maximum at wavelengths, thus it can be used as an easy and straightforward method to accurately estimated spectra. Three kinds of possible configurations of the CNDs are named configuration-1, configuration-2, and configuration-3 based on the precursors, as shown in Fig. 3(a). The LUMO and the HOMO of the three kind of configurations are achieved based on the computationally results, as shown in Fig. 3(b). The gaps of the three configurations are 4.362, 3.939, and 2.859 eV, and only gap of the configuration-3 agree with the CNDs. In addition, for configuration-1 and configuration-2, the overlap between LUMO and HOMO are small, thus the emission will be weak. The LUMO of configuration-3 is distributed over the whole polyimide and part of oxygen atoms linked with polyimide. Whereas, the electron distributions of the corresponding HOMO are dominantly localized on almost every group and atom. Therefore, a partial HOMO-LUMO separation is realized which results in potential bipolar charger transport properties and a larger oscillator strength. Compared to configuration-1 and configuration-2 molecule in which the HOMO and LUMO are almost completely spatially separated, such frontier molecular orbital feature of configuration-3 leads to effective electronic recombination, and obvious overlap is more likely to endow it an efficient luminescence emitter. Additionally, theoretical calculated absorption and emission spectra of the three configurations are shown in Fig. 3(c). The absorption peaks of configuration-1 and configuration-2 are 190, 215 nm,

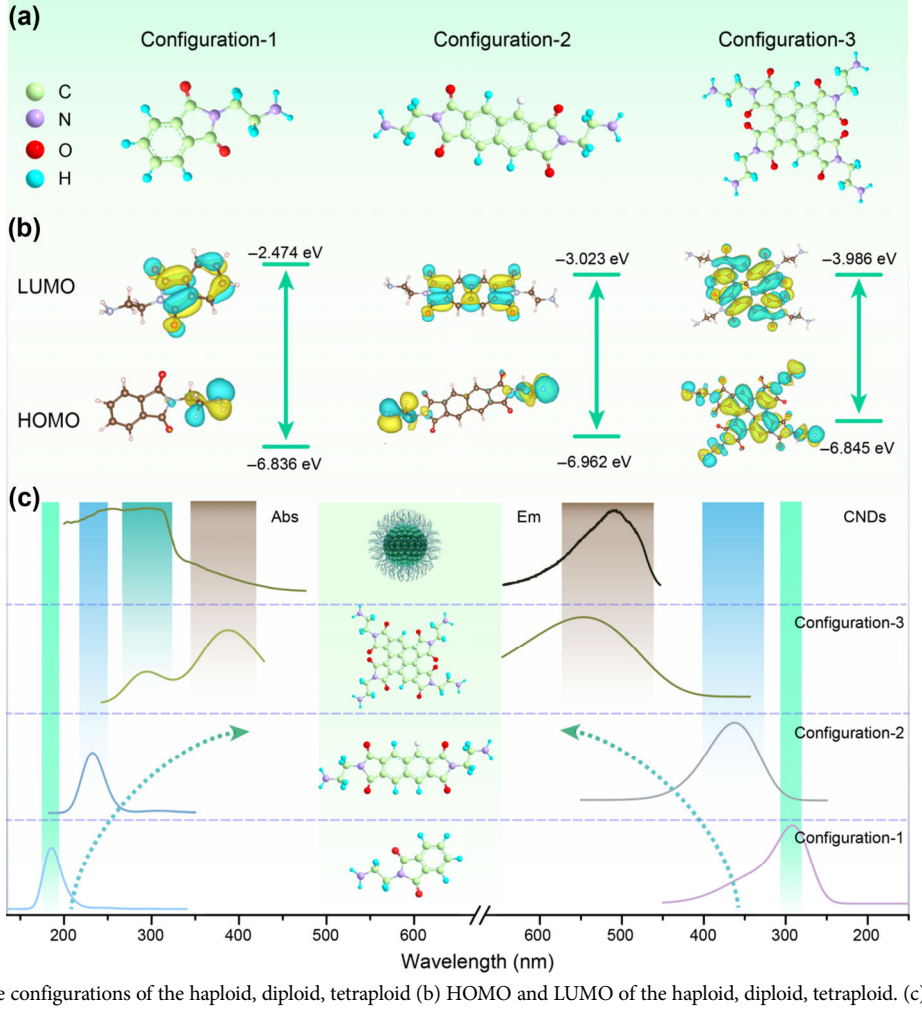

Figure 3 (a) The three configurations of the haploid, diploid, tetraploid (b) HOMO and LUMO of the haploid, diploid, tetraploid. (c) Calculated absorption and emission spectra of the three configurations and the corresponding absorption and emission spectra of the CNDs.

whereas the spectrum of the configuration-3 show absorption bands at around 290–385 nm agrees well with the experimental peak in the Fig. 3(c) (left). Green emission peak can be observed from the calculated spectrum of configuration-3, which can also be observed from the PL spectrum of the CNDs as shown in the Fig. 3(c) (right). Configuration-3 and CNDs have similar emissive and absorption properties, from which we can predict that the CNDs are mainly composed of configuration-3 molecule.

To investigate optical properties of CNDs, excitation-emission contour plots of the CNDs in ethanol solution are displayed in Fig. 4(a), and the emission of the CNDs remains almost unchanged when varying the excitation wavelength, indicating the existence of just one kind of luminescent center in the CNDs. It is reported that excitation-dependent emission behavior that is frequently in CNDs is related to molecular state, thus the excitation-independent emission observed in our case may originate from the core-state carrier radiative recombination of the CNDs. UV–Vis absorption spectra show that the CNDs have similar absorption spectra in different polar solutions, as shown in Fig. 4(b). The absorption wavelength range with a prominent peak at around 270 to 320 nm is demonstrated to undergo a transition of the conjugated C=C band [50, 51]. As expected, this absorption band shows gradual bathochromic (red) shift of 7 nm with increase in polarity of polar protic solvents like ethanol, methanol, and isopropanol. On the contrary, a hypochromic (blue) shift of 3 nm has been observed in aprotic solvents like dimethylformamide (DMF), dimethyl sulfoxide (DMSO), and tetrahydrofuran (THF). The blue shift indicates transition, as shown in Fig. 4(b). Therefore, it is speculated that both transition contribute to the emission of the CNDs, leading to the broad absorption band at 270 to 320 nm. To further clarify the luminescence mechanism of the CNDs, the PL decay curves of the CNDs collected at 505 nm show the same decay trend in different polar solvents, as shown in Fig. 4(c), indicating the carriers of the CNDs have identical dynamics process, which can be assigned to the intrinsic emission of the CNDs. In addition, PL decay curve of the CNDs is very close to the single-exponential function shape, and the lifetime of the CNDs is around 6.0 ns. Time-resolved fluorescence spectra were measured to further evaluate the decay lifetime of the CNDs in their emission region. The carrier lifetime induced from the time-resolved spectra of the CNDs is about 6.0 ns as shown in Fig. 4(d). The spectra variation of the PL spectra at various time are shown in Fig. 4(e). Notably, no obvious change of spectral shape was evidenced, which reveals an essentially time-independent spectral shape of the PL emission. The temperature-dependent PL spectra of the CNDs are shown in Fig. S6(a) in the ESM. The PL intensity of CNDs shows a slight decrease with increase of temperature, and the decrease can be ascribed to thermally activated exciton dissociation and nonradiative trapping. The integrated PL emission intensities as a function of temperature (90–290 K) were plotted by using the following equation

$$I(\mathrm{T}) = \frac{I_0}{1 + Ae^{\frac{-E_b}{k_b T}}} \quad (1)$$

Where I_0 is the intensity at 0 K, E_b is the exciton binding energy,

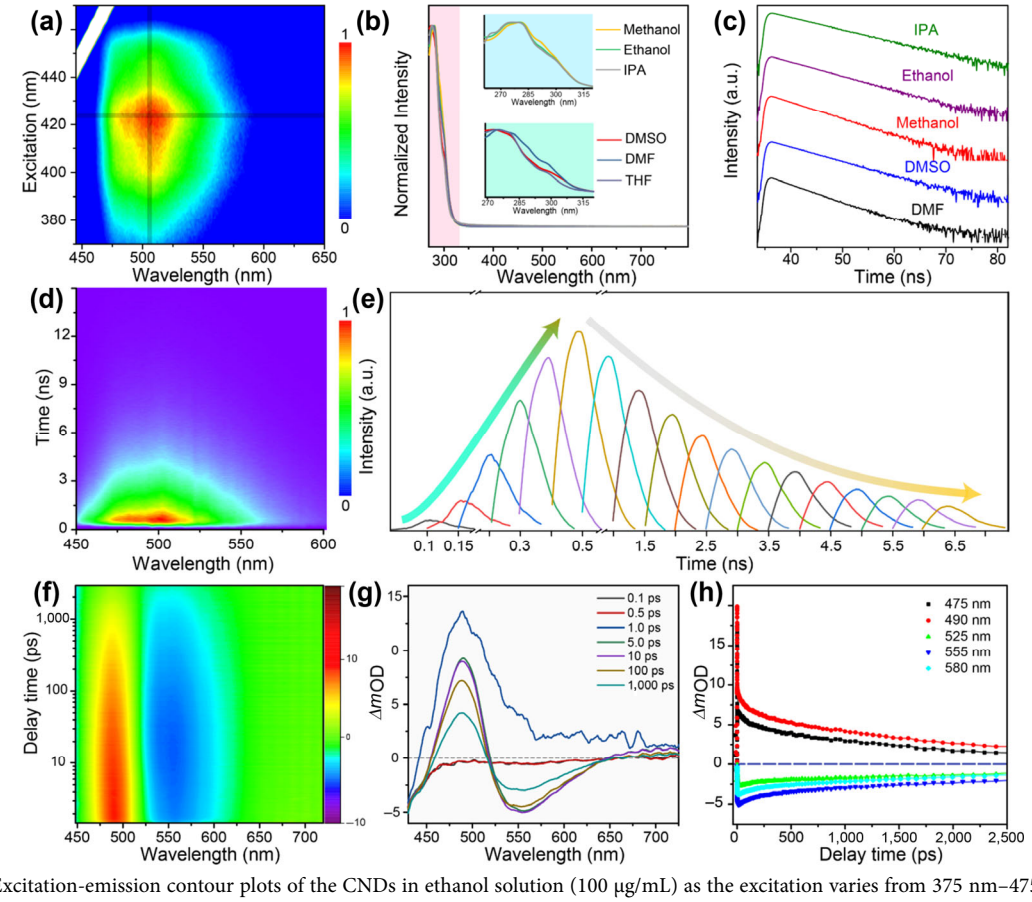

Figure 4 (a) Excitation-emission contour plots of the CNDs in ethanol solution (100 μg/mL) as the excitation varies from 375 nm–475 nm. (b) UV–vis absorption spectra of the CNDs in different polar solvents (50 μg/mL). (c) Time resolved decay curves of the CNDs recorded at 505 nm. (d) Time resolved luminescence contour of the CNDs in ethanol (100 μg/mL). (e) The fluorescence spectra of the CNDs recorded at various time. (f) 2D top-view transient absorption (TA) spectrum of the CNDs with a pump wavelength of 400 nm. (g) TA spectra of the CNDs at indicated delay times from 0.5 to 1,000 ps. (h) TA kinetic process of the CNDs probed at different wavelengths.

and k_B is the Boltzmann constant [52]. From the fitting result analysis, the CNDs have a relatively large exciton binding energy of 89.8 meV, indicating the high thermostability and the minimal nonradiative recombination centers or defects (Fig. S6 (b) in the ESM). To illustrate the emission nature of the CNDs more clearly, single-particle PL imaging experiments were carried out under the excitation of 405 nm lamp (Fig. S7(a) in the ESM). The fluorescence emission intensity from each CND is also highly consistent, are indicated in Fig. S7(b) in the ESM. Furthermore, the emission intensity of the CNDs decreases a little under the UV light illumination for 5 days, indicating that the CNDs have high ambient stability and excellent anti-bleaching properties (Fig. S(8) in the ESM). To explore the recombination dynamics of the CNDs further, femtosecond transient absorption (fs-TA) spectroscopy measurement was carried out under excitation of 400 nm. TA spectra of the CNDs probe at 400–900 nm, with scan delay times from 0.1 to 1,500 ps, and the correspond contour plots are shown in Fig. 4(f). The negative (blue) features from 530 to 600 nm correspond to the stimulated emission (SE) and the relatively weaker negative features from 420 to 445 nm correspond to the ground state bleaching (GSB). The positive (red) features from 465 to 510 nm correspond to the excited state absorption (ESA). The TA spectra at different time delays and the kinetics of each featured wavelength in terms of delay time are shown in Figs. 4(g) and 4(h). To explore the detailed relaxation channels of the excited carriers, we used 3 exponent decay functions to fit the TA spectra. The fitted decay associated difference spectra (DADS) are shown in Fig. S9(a) in the ESM. The fitted lifetimes of carriers are 0.23, 46.1, and 2.07 ns, respectively. On the basis of the DADS, one can ascribe the three components to the corresponding relaxation channels: After excitation, a lot of hot carriers dissipate their energy in the same location; a large amount of hot carriers releases their redundant energy by photon scattering within 0.23 ps. Part of the cooled carriers, whose dynamics is distributed at about 480 nm, will undergo nonradiative transition to ground state within 46.1 ps. The remaining part will emit fluorescence (2.07 ns) via recombination of electrons and holes, and all of the processes are illustrated in Fig. S9(b) in the ESM.

In addition, the CNDs show good fluorescence and biocompatibility, thus they can be used in the field of cell imaging. The two-photon fluorescence properties of CNDs under the excitation of 800 nm were investigated using a femtosecond pulsed laser (Fig. S10(a) in the ESM), and the 2-photon excitation process of the CNDs is illustrated in the bottom of Fig. S10(a) in the ESM. The fluorescence spectra of the CNDs under the excitation of 800 nm are shown in Fig. S10(b) in the ESM, and the emission intensity increases with the excitation power. The slope of the fluorescence intensity versus excitation power density is 1.9, indicating 2-photon excited fluorescence of the CNDs (Fig. S10(c) in the ESM). The two-photon fluorescence property of the CNDs inspires us to investigate their application in cellular imaging. The cytotoxicity of the CNDs has been evaluated through the Cell Counting Kit-8 (CCK8) assays before the cellular imaging experiment, as shown in Fig. S10(d) in the ESM. The cytotoxicity result shows that the DC 2.4 cell viabilities can maintain over 92% after 24 h incubation with the CNDs, even the concentration of the CNDs is up to 200 ug/ml, revealing the good dispersibility, serum solubility and low cytotoxicity of the CNDs. Figures S9(e) and S9(g) in the ESM show the fluorescence images of the saccharomyces cerevisiae cells under excitation different wavelengths (405 nm in one-photon excitation mode, 800 nm in two-photon excitation mode). Bright emission of the cells can be observed, indicating the CNDs are distributed into cytoplasm of the cerevisiae cells uniformly. Interestingly, the bright fluorescence of the CNDs in the cell can be still observed under the excitation of 900 nm, as shown in Fig. S11 in the ESM. The corresponding merged images of fluorescence images and bight field images are shown in Figs. S9(f) and S9(g) in the ESM, and they coincide each other well. The result indicates that the CNDs are capable of emissive agent with low cytotoxicity.

Interestingly, in addition to fluorescence, the CNDs show room temperature phosphorescence property. In order to investigate the phosphorescence mechanism of the CNDs, the excitation state energies, spin-orbit couplings (ξ), and nature transition orbitals of the CNDs with configuration-3 structure are calculated, as shown in Fig. 5(a). In the calculated SOC coefficients of S_1 state with triplet states ξ (S_1, T_n) of the CNDs are 0.570, 0.041, 0.319, 0.390, 0.502, thus non-radiation transition between singlet and triplet states occurs mainly between S_1 and T_1 state. UV/Vis absorption spectra (Fig. S12 in the ESM) reveal the strong transition of C=O bonds of the CNDs at about 330 to 420 nm in the solid state, indicating that there is strong coupling in aggregated CNDs. Notably, the effective stabilization of triplet excited states through strong coupling in aggregated CNDs can promote the generation of intrinsic triplet carriers through ISC [53]. The phosphorescence excitation peak at around 360 nm can be observed in Fig. S13 in the ESM and this is in good accordance with the CNDs absorption spectrum. The excitation-phosphorescence contour plots of the CNDs are shown in Fig. 5(b). Emission peak at around 505 nm can be observed and the optimum excitation wavelength is located at around 410 nm. The phosphorescence and fluorescence spectra of the CNDs are similar at room temperature, and the corresponding images of the CNDs under daylight, UV illumination and after UV illumination are shown in the inset of Fig. 5(c). The energy gap between the S_1 and T_1 excited states (ΔE_{ST}) have been further studied. The phosphorescence spectrum measured at 77 K shows an emission band at 515 nm, (blue line in Fig. 5(d)) and the fluorescence peak located at around 505 nm, a ΔE_{ST} value of 0.05 eV can be obtained. The small energy gap may make the ISC process from the S_1 to T_1 state possible, thus facilitating the generation of phosphorescence phenomenon. Time resolved decay spectra reveal the presence of long-lived species with lifetimes 193 ms at room temperature (Fig. S14(a) in the ESM). Thus, bright green phosphorescence can be observed nearly 5 s after removing the irradiation source, as shown in Fig. S14(b) in the ESM. The temperature dependent transient photoluminescence decay plots of the CNDs from 78 to 353 K are shown in Fig. 5(e). It can be found that the lifetime is strongly independent of temperature, and this phenomenon may be associated with the stability of the triplet excited states. The lower temperatures will "freeze" atoms inside of the CNDs and non-radiation channels of the triplet excited states are thus blocked. The variation of the lifetimes versus temperature is shown in Fig. 5(f), a strong temperature dependence of the carrier lifetime is observed. The lifetime of the CNDs show a sharp decrease at around 280 K, indicating the CNDs can be used as temperature sensor. In addition, it has been confirmed that the vibration-limited CNDs had a long carrier lifetime (1.13 s), whereas the dispersed CNDs had a very short lifetime (6 ns), as shown in Fig. S15 in the ESM. The results show that triplet excitons can only be stable in frozen CNDs, and they become more stable at low temperature. In order to verify the above speculation, a clear

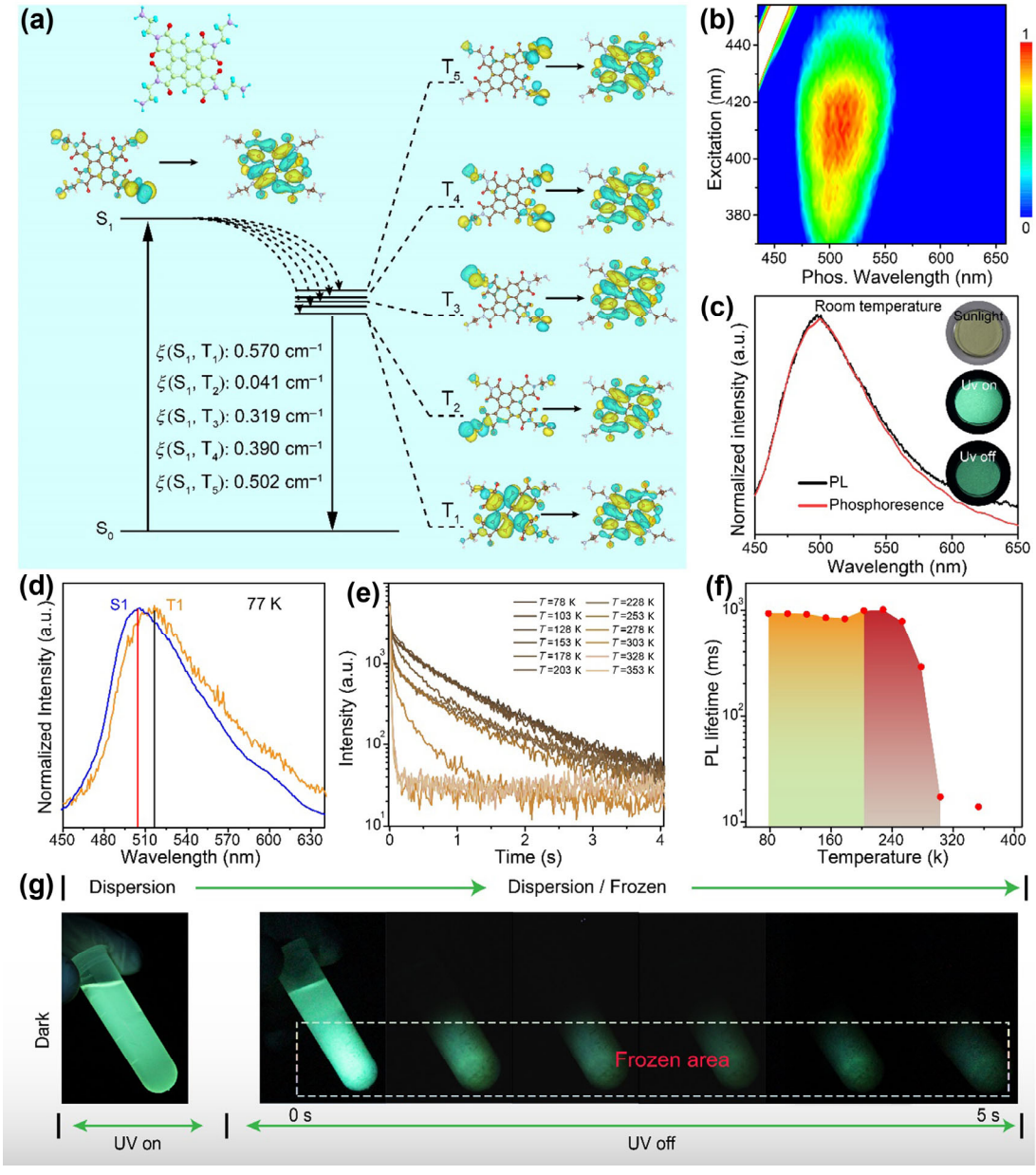

Figure 5 (a) Calculated excitation energies, spin-orbit couplings (ξ) and nature transition orbitals for tetraploid molecules. (b) Excitation-phosphorescence emission contour of the CNDs powders as the excitation varies from 375–465 nm. (c) Photoluminescence spectrum (black line) and phosphorescence spectrum (red line) of CNDs excited under 365 nm at room temperature, the inset shows the photographs of CNDs under sunlight, excited with a 365 nm UV lamp on and off. (d) The steady-state (blue line) and phosphorescence (green line) spectra of the purified mother liquids of CNDs excited under 370 nm at 77 K. (e) Temperature-dependent transient photoluminescence decay of the CNDs powders at 505 nm. (f) Fluorescence lifetime fitting curve of the CNDs from 77 to 353 K. (g) The photographs of the conversion of fluorescence emission into a phosphorescence among frozen aggregate CNDs and dispersed CNDs.

and transparent DMSO solution of the CNDs is displayed in the left of Fig. 5(g), and green fluorescence can be observed under UV illumination. The bottom solution in the centrifuge tube was frozen by cooling, thereby the dispersed CNDs was fixed within the frozen DMSO, and one can found that the bottom CNDs showed bright phosphorescence after cessation UV illumination, as shown in right of Fig. 5(g). The above results indicate that triplet excitons deactivation is mainly through the rotation and vibration of the atoms of CNDs. In addition, the phosphorescence intensity of the CNDs can maintain constant after UV illumination for 5 days, and it can be activated repeatedly with no obvious decrease, indicating the good photo stability of the CNDs (Fig. S16 in the ESM).

The long lifetime phosphorescence of the CNDs inspired us to investigate their application in the fields of information encryption and decryption. By adopting the CNDs and commercial red fluorescent highlighters, graphic and information encryption have been proposed and demonstrated, and all of the pattern and encoding process are shown in Fig. 6(a). A hidden security feature information was written on a non-luminescent background paper using the CNDs, and then commercial fluorescent pen was used to produce a pattern, the overlap area is the coding area. Under UV illumination, the produced patterns only show red emission because the commercial phosphor is brighter than the CNDs, and the corresponding spectra of the coding area of the pattern are shown in Fig. 6(b). Graphic and text pattern were coded according to the above designed idea. The patterns are visible under illumination of 365 nm light. Only the coding area within the patterns can be observed after cessation UV illumination as a

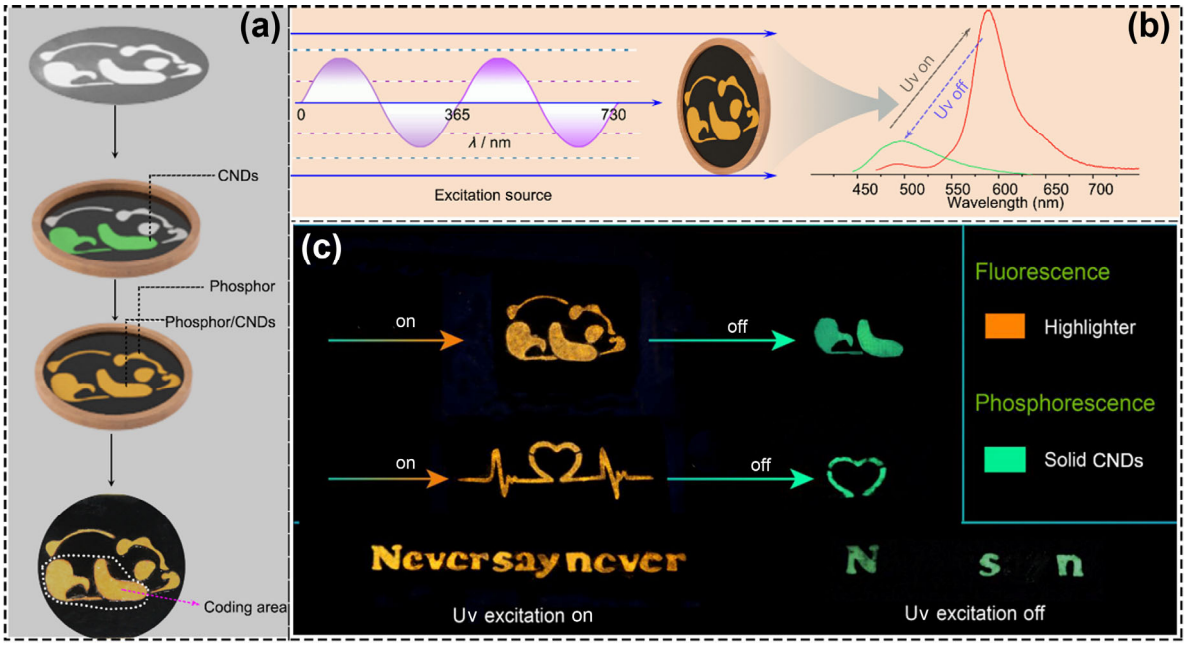

Figure 6 (a) Schematic diagram of patterning by combining the CNDs and commercial highlighters. (b) Schematic of the pattern under UV illumination (left) and the corresponding spectra of coding area of the pattern with and without UV illumination. (c) Photographs of graphic and information encryption using the CND and commercial highlighters as ink.

result of the intrinsic different emission between fluorescence and phosphorescence are shown in Fig. 6(c). This demonstration indicates the CNDs can be worked as encrypted ink in some specific scene.

Conclusions

In summary, phosphorescent CNDs with a large-scale production synthesized by a self-exothermic reaction at room temperature has been demonstrated for the first time. The as-prepared CNDs own fluorescence and phosphorescence properties, which are comparable with that synthesized by solvothermal and microwave-assisted heating methods. Detailed experimental and computational investigations indicate the effective ISC from $^1(\pi, \pi^*)$ or $^3(n, \pi^*)$ facilities the phosphorescence of the CNDs. Tunable phosphorescence lifetimes from 193 ms to 1.13 s at different temperatures have been observed from the CNDs, and information encryption by using the CNDs as phosphorescent ink has been demonstrated. Considering that RTP materials with a long phosphorescence lifetime and efficiency are highly desired, increasing the phosphorescence lifetime and efficiency of the CNDs will further extend their applications. The result reported in this paper may drive the development of room temperature and large-scale synthesis of phosphorescent CNDs.

Acknowledgements

This work was supported by the National Natural Science Foundation of China (Nos. 11904326, U1804155, and U1604263), China Postdoctoral Science Foundation (Nos. 2019TQ0287, and 2019M662510), the Chemical Dynamics Research Center (No. 21688102), the Key Technology Team of the Chinese Academy of Sciences (No. GJJSTD20190002).

Electronic Supplementary Material: Supplementary material (further details of the experimental section and characterization) is available in the online version of this article at https://doi.org/10.1007/s12274-020-3204-z

References

[1] Gong, Y. Y.; Chen, G.; Peng, Q.; Yuan, W. Z.; Xie, Y. J.; Li, S. H.; Zhang, Y. M.; Tang, B. Z. Achieving persistent room temperature phosphorescence and remarkable mechanochromism from pure organic luminogens. *Adv. Mater.* **2015**, *27*, 6195–6201.

[2] Cai, S. Z.; Shi, H. F.; Li, J. W.; Gu, L.; Ni, Y.; Cheng, Z. C.; Wang, S.; Xiong, W. W.; Li, L.; An, Z. F. et al. Visible-light-excited ultralong organic phosphorescence by manipulating intermolecular interactions. *Adv. Mater.* **2017**, *29*, 1701244

[3] Sun, H. B.; Liu, S. J.; Lin, W. P.; Zhang, K. Y.; Lv, W.; Huang, X.; Huo, F. W.; Yang, H. R.; Jenkins, G.; Zhao, Q. et al. Smart responsive phosphorescent materials for data recording and security protection. *Nat. Commun.* **2014**, *5*, 3601.

[4] An, Z. F.; Zheng, C.; Tao, Y.; Chen, R. F.; Shi, H. F.; Chen, T.; Wang, Z. X.; Li, H. H.; Deng, R. R.; Liu, X. G. et al. Stabilizing triplet excited states for ultralong organic phosphorescence. *Nat. Mater.* **2015**, *14*, 685–690.

[5] He, Z. K.; Zhao, W. J.; Lam, J. W. Y.; Peng, Q.; Ma, H. L.; Liang, G. D.; Shuai, Z. G.; Tang, B. Z. White light emission from a single organic molecule with dual phosphorescence at room temperature. *Nat. Commun.* **2017**, *8*, 416.

[6] Liang, Y. C.; Gou, S. S.; Liu, K. K.; Wu, W. J.; Guo, C. Z.; Lu, S. Y.; Zang, J. H.; Wu, X. Y.; Lou, Q.; Dong, L. et al. Ultralong and efficient phosphorescence from silica confined carbon nanodots in aqueous solution. *Nano Today* **2020**, *34*, 100900.

[7] Li, D. F.; Lu, F. F.; Wang, J.; Hu, W. D.; Cao, X. M.; Ma, X.; Tian, H. Amorphous metal-free room-temperature phosphorescent small molecules with multicolor photoluminescence via a host-guest and dual-emission strategy. *J. Am. Chem. Soc.* **2018**, *140*, 1916–1923.

[8] Liu, K. K.; Liu, Q.; Yang, D. W.; Liang, Y. C.; Sui, L. Z.; Wei, J. Y.; Xue, G. W.; Zhao, W. B.; Wu, X. Y.; Dong, L. et al. Water-induced $MAPbBr_3$@PbBr(OH) with enhanced luminescence and stability. *Light: Sci. Appl.* **2020**, *9*, 44.

[9] Li, X. M.; Wu, Y.; Zhang, S. L.; Cai, B.; Gu, Y.; Song, J. Z.; Zeng, H. B. $CsPbX_3$ quantum dots for lighting and displays: Room-temperature synthesis, photoluminescence superiorities, underlying origins and white light-emitting diodes. *Adv. Funct. Mater.* **2016**, *26*, 2435– 2445.

[10] Wei, J. Y.; Lou, Q.; Zang, J. H.; Liu, Z. Y.; Ye, Y. L.; Shen, C. L.; Zhao, W. B.; Dong, L.; Shan, C. X. Scalable Synthesis of Green Fluorescent Carbon Dot Powders with Unprecedented Efficiency.

Adv. Opt. Mater. **2020**, *8*, 1901938.
[11] Zheng, Y. B.; Liu, H. Y.; Li, J. X.; Xiang, J.; Panmai, M.; Dai, Q. F.; Xu, Y.; Tie, S. L.; Lan, S. Controllable formation of luminescent carbon quantum dots mediated by the Fano resonances formed in oligomers of gold nanoparticles. *Adv. Mater.* **2019**, *31*, 1901371.
[12] Zhang, J.; Yuan, Y.; Gao, M. L.; Han, Z.; Chu, C. Y.; Li, Y. G.; van Zijl, P. C. M.; Ying, M. Y.; Bulte, J. W. M.; Liu, G. S. Carbon dots as a new class of diamagnetic chemical exchange saturation transfer (diaCEST) MRI contrast agents. *Angew. Chem., Int. Ed.* **2019**, *58*, 9871–9875.
[13] Li, H. X.; Yan, X.; Kong, D. S.; Jin, R.; Sun, C. Y.; Du, D.; Lin, Y. H.; Lu, G. Y. Recent advances in carbon dots for bioimaging applications. *Nanoscale Horiz.* **2020**, *5*, 218–234.
[14] Ye, X. X.; Xiang, Y. H.; Wang, Q. R.; Li, Z.; Liu, Z. H. A red emissive two-photon fluorescence probe based on carbon dots for intracellular pH detection. *Small* **2019**, *15*, 1901673.
[15] Wei, X. J.; Li, L.; Liu, J. L.; Yu, L. D.; Li, H. B.; Cheng, F.; Yi, X. T.; He, J. M.; Li, B. S. Green synthesis of fluorescent carbon dots from gynostemma for bioimaging and antioxidant in Zebrafish. *ACS Appl. Mater. Interfaces* **2019**, *11*, 9832–9840.
[16] Sun, S.; Chen, J. Q.; Jiang, K.; Tang, Z. D.; Wang, Y. H.; Li, Z. J.; Liu, C. B.; Wu, A. G.; Lin, H. W. Ce6-modified carbon dots for multimodal-imaging-guided and single-NIR-laser-triggered photothermal/photodynamic synergistic cancer therapy by reduced irradiation power. *ACS Appl. Mater. Interfaces* **2019**, *11*, 5791–5803.
[17] Liu, K. K.; Song, S. Y.; Sui, L. Z.; Wu, S. X.; Jing, P. T.; Wang, R. Q.; Li, Q. Y.; Wu, G. R.; Zhang, Z. Z.; Yuan, K. J. et al. Efficient red/near-infrared-emissive carbon nanodots with multiphoton excited upconversion fluorescence. *Adv. Sci.* **2019**, *6*, 1900766.
[18] Zhi, B.; Cui, Y.; Wang, S. Y.; Frank, B. P.; Williams, D. N.; Brown, R. P.; Melby, E. S.; Hamers, R. J.; Rosenzweig, Z.; Fairbrother, D. H. et al. Malic acid carbon dots: From super-resolution live-cell imaging to highly efficient separation. *ACS Nano* **2018**, *12*, 5741–5752.
[19] Shen, C. L.; Lou, Q.; Zang, J. H.; Liu, K. K.; Qu, S. N.; Dong, L.; Shan, C. X. Near-infrared chemiluminescent carbon nanodots and their application in reactive oxygen species bioimaging. *Adv. Sci.* **2020**, *7*, 1903525.
[20] Shen, C. L.; Lou, Q.; Lv, C. F.; Zang, J. H.; Qu, S. N.; Dong, L.; Shan, C. X. Bright and Multicolor Chemiluminescent Carbon Nanodots for Advanced Information Encryption. *Adv. Sci.* **2019**, *6*, 1802331.
[21] Li, Y. B.; Bai, G. X.; Zeng, S. J.; Hao, J. H. Theranostic carbon dots with innovative NIR-II emission for *in vivo* renal-excreted optical imaging and photothermal therapy. *ACS Appl. Mater. Interfaces* **2019**, *11*, 4737–4744.
[22] Song, S. Y.; Liu, K. K.; Wei, J. Y.; Lou, Q.; Shang, Y.; Shan, C. X. Deep-ultraviolet emissive carbon nanodots. *Nano Lett.* **2019**, *19*, 5553– 5561.
[23] Feng, T. L.; Zeng, Q. S.; Lu, S. Y.; Yan, X. J.; Liu, J. J.; Tao, S. Y.; Yang, M. X.; Yang, B. Color-tunable carbon dots possessing solid-state emission for full-color light-emitting diodes applications. *ACS Photonics* **2018**, *5*, 502–510.
[24] Yuan, F. L.; Wang, Y. K.; Sharma, G.; Dong, Y. T.; Zheng, X. P.; Li, P. C.; Johnston, A.; Bappi, G.; Fan, J. Z.; Kung, H. et al. Bright high-colour-purity deep-blue carbon dot light-emitting diodes via efficient edge amination. *Nat. Photonics* **2020**, *14*, 171–176.
[25] Semeniuk, M.; Yi, Z. H.; Poursorkhabi, V.; Tjong, J.; Jaffer, S.; Lu, Z. H.; Sain, M. Future perspectives and review on organic carbon dots in electronic applications. *ACS Nano* **2019**, *13*, 6224–6255.
[26] Jiang, K.; Gao, X. L.; Feng, X. Y.; Wang, Y. H.; Li, Z. J.; Lin, H. W. Carbon dots with dual-emissive, robust, and aggregation-induced room-temperature phosphorescence characteristics. *Angew. Chem., Int. Ed.* **2020**, *59*, 1263–1269.
[27] Tang, G. Q.; Zhang, K.; Feng, T. L.; Tao, S. Y.; Han, M.; Li, R.; Wang, C. C.; Wang, Y.; Yang, B. One-step preparation of silica microspheres with super-stable ultralong room temperature phosphorescence. *J. Mater. Chem. C* **2019**, *7*, 8680–8687.
[28] Lin, C. J.; Zhuang, Y. X.; Li, W. H.; Zhou, T. L.; Xie, R. J. Blue, green, and red full-color ultralong afterglow in nitrogen-doped carbon dots. *Nanoscale* **2019**, *11*, 6584–6590.
[29] Li, W.; Wu, S. S.; Xu, X. K.; Zhuang, J. L.; Zhang, H. R.; Zhang, X. J.; Hu, C. F.; Lei, B. F.; Kaminski, C. F.; Liu, Y. Q. Carbon dot-silica nanoparticle composites for ultralong lifetime phosphorescence imaging in tissue and cells at room temperature. *Chem. Mater.* **2019**, *31*, 9887–9894.
[30] Li, Q. J.; Zhou, M.; Yang, Q. F.; Wu, Q.; Shi, J.; Gong, A. H.; Yang, M. Y. Efficient room-temperature phosphorescence from nitrogen-doped carbon dots in composite matrices. *Chem. Mater.* **2016**, *28*, 8221–8227.
[31] Liu, J. C.; Zhang, H. Y.; Wang, N.; Yu, Y.; Cui, Y. Z.; Li, J. Y.; Yu, J. H. Template-modulated afterglow of carbon dots in zeolites: Room-temperature phosphorescence and thermally activated delayed fluorescence. *ACS Mater. Lett.* **2019**, *1*, 58–63.
[32] Li, W.; Zhou, W.; Zhou, Z. S.; Zhang, H. R.; Zhang, X. J.; Zhuang, J. L.; Liu, Y. L.; Lei, B. F.; Hu, C. F. A universal strategy for activating the multicolor room-temperature afterglow of carbon dots in a boric acid matrix. *Angew. Chem., Int. Ed.* **2019**, *58*, 7278–7283.
[33] Zhang, J. Y.; Lu, X. M.; Tang, D. D.; Wu, S. H.; Hou, X. D.; Liu, J. W.; Wu, P. Phosphorescent carbon dots for highly efficient oxygen photosensitization and as photo-oxidative nanozymes. *ACS Appl. Mater. Interfaces* **2018**, *10*, 40808–40814.
[34] Tao, S. Y.; Lu, S. Y.; Geng, Y. J.; Zhu, S. J.; Redfern, S. A. T.; Song, Y. B.; Feng, T. L.; Xu, W. Q.; Yang, B. Design of metal-free polymer carbon dots: A new class of room-temperature phosphorescent materials. *Angew. Chem., Int. Ed.* **2018**, *57*, 2393–2398.
[35] Wang, C.; Chen, Y. Y.; Xu, Y. L.; Ran, G. X.; He, Y. M.; Song, Q. J. Aggregation-induced room-temperature phosphorescence obtained from water-dispersible carbon dot-based composite materials. *ACS Appl. Mater. Interfaces* **2020**, *12*, 10791–10800.
[36] Jiang, K.; Hu, S. Z.; Wang, Y. C.; Li, Z. J.; Lin, H. W. Photo-stimulated polychromatic room temperature phosphorescence of carbon dots. *Small* **2020**, *16*, 2001909.
[37] De Medeiros, T. V.; Manioudakis, J.; Noun, F.; Macairan, J. R.; Victoria, F.; Naccache, R. Microwave-assisted synthesis of carbon dots and their applications. *J. Mater. Chem. C* **2019**, *7*, 7175–7195.
[38] Miao, X.; Qu, D.; Yang, D. X.; Nie, B.; Zhao, Y. K.; Fan, H. Y.; Sun, Z. C. Synthesis of carbon dots with multiple color emission by controlled graphitization and surface functionalization. *Adv. Mater.* **2018**, *30*, 1704740.
[39] Kenry; Chen, C. J.; Liu, B. Enhancing the performance of pure organic room-temperature phosphorescent luminophores. *Nat. Commun.* **2019**, *10*, 2111.
[40] Lower, S. K.; El-Sayed, M. A. The triplet state and molecular electronic processes in organic molecules. *Chem. Rev.* **1966**, *66*, 199–241.
[41] Jiang, K.; Wang, Y. H.; Cai, C. Z.; Lin, H. W. Conversion of carbon dots from fluorescence to ultralong room-temperature phosphorescence by heating for security applications. *Adv. Mater.* **2018**, *30*, 1800783.
[42] Zhao, W. J.; He, Z. K.; Lam, J. W. Y.; Peng, Q.; Ma, H. L.; Shuai, Z. G.; Bai, G. X.; Hao, J. H.; Tang, B. Z. Rational molecular design for achieving persistent and efficient pure organic room-temperature phosphorescence. *Chem* **2016**, *1*, 592–602.
[43] Sun, C.; Zhang, Y.; Ruan, C.; Yin, C. Y.; Wang, X. Y.; Wang, Y. D.; Yu, W. W. Efficient and stable white LEDs with silica-coated inorganic perovskite quantum dots. *Adv. Mater.* **2016**, *28*, 10088–10094.
[44] Li, D.; Jing, P. T.; Sun, L. H.; An, Y.; Shan, X. Y.; Lu, X. H.; Zhou, D.; Han, D.; Shen, D. Z.; Zhai, Y. C. et al. Near-infrared excitation/emission and multiphoton-induced fluorescence of carbon dots. *Adv. Mater.* **2018**, *30*, 1705913.
[45] Vallan, L.; Urriolabeitia, E. P.; Ruipérez, F.; Matxain, J. M.; Canton-Vitoria, R.; Tagmatarchis, N.; Benito, A. M.; Maser, W. K. Supramolecular-enhanced charge transfer within entangled polyamide chains as the origin of the universal blue fluorescence of polymer carbon dots. *J. Am. Chem. Soc.* **2018**, *140*, 12862–12869.
[46] Geng, X.; Sun, Y. Q.; Li, Z. H.; Yang, R.; Zhao, Y. M.; Guo, Y. F.; Xu, J. J.; Li, F. T.; Wang, Y.; Lu, S. Y. et al. Retrosynthesis of tunable fluorescent carbon dots for precise long-term mitochondrial tracking. *Small* **2019**, *15*, 1901517.
[47] Yang, H. Y.; Liu, Y. L.; Guo, Z. Y.; Lei, B. F.; Zhuang, J. L.; Zhang, X. J.; Liu, Z. M.; Hu, C. F. Hydrophobic carbon dots with blue

dispersed emission and red aggregation-induced emission. *Nat. Commun*. **2019**, *10*, 1789.

[48] Lu, S. Y.; Sui, L. Z.; Liu, J. J.; Zhu, S. J.; Chen, A. M.; Jin, M. X.; Yang, B. Near-infrared photoluminescent polymer-carbon nanodots with two-photon fluorescence. *Adv. Mater*. **2017**, *29*, 1603443.

[49] Lu, S. Y.; Xiao, G. J.; Sui, L. Z.; Feng, T. L.; Yong, X.; Zhu, S. J.; Li, B. J.; Liu, Z. Y.; Zou, B.; Jin, M. X. et al. Piezochromic carbon dots with two-photon fluorescence. *Angew. Chem., Int. Ed*. **2017**, *56*, 6187–6191.

[50] Sharma, A.; Gadly, T.; Neogy, S.; Ghosh, S. K.; Kumbhakar, M. Molecular Origin and Self-Assembly of Fluorescent Carbon Nanodots in Polar Solvents. *J. Phys. Chem. Lett*. **2017**, *8*, 1044–1052.

[51] Reckmeier, C. J.; Wang, Y.; Zboril, R.; Rogach, A. L. Influence of doping and temperature on solvatochromic shifts in optical spectra of carbon dots. *J. Phys. Chem. C* **2016**, *120*, 10591–10604.

[52] Yuan, F. L.; Yuan, T.; Sui, L. Z.; Wang, Z. B.; Xi, Z. F.; Li, Y. C.; Li, X. H.; Fan, L. Z.; Tan, Z. A.; Chen, A. M. et al. Engineering triangular carbon quantum dots with unprecedented narrow bandwidth emission for multicolored LEDs. *Nat. Commun*. **2018**, *9*, 2249.

[53] Liang, Y. C.; Shang, Y.; Liu, K. K.; Liu, Z.; Wu, W. J.; Liu, Q.; Zhao, Q.; Wu, X. Y.; Dong, L.; Shan, C. X. Water-induced ultralong room temperature phosphorescence by constructing hydrogen-bonded networks. *Nano Res*. **2020**, *13*, 875–881.